



ARTICLE OPEN

Schnurri-3 inhibition rescues skeletal fragility and vascular skeletal stem cell niche pathology in the OIM model of osteogenesis imperfecta

Na Li^{1,2}, Baohong Shi^{1,2}, Zan Li^{1,3}, Jie Han¹, Jun Sun^{1,4}, Haitao Huang¹, Alisha R. Yallowitz⁵, Seoyeon Bok⁵, Shuang Xiao¹, Zuoxing Wu¹, Yu Chen¹, Yan Xu³, Tian Qin^{1,3}, Rui Huang¹, Haiping Zheng^{1,2}, Rong Shen², Lin Meng⁶, Matthew B. Greenblatt^{1,2,5} and Ren Xu^{1,2}

Osteogenesis imperfecta (OI) is a disorder of low bone mass and increased fracture risk due to a range of genetic variants that prominently include mutations in genes encoding type I collagen. While it is well known that OI reflects defects in the activity of bone-forming osteoblasts, it is currently unclear whether OI also reflects defects in the many other cell types comprising bone, including defects in skeletal vascular endothelium or the skeletal stem cell populations that give rise to osteoblasts and whether correcting these broader defects could have therapeutic utility. Here, we find that numbers of skeletal stem cells (SSCs) and skeletal arterial endothelial cells (AECs) are augmented in *Col1a2*^{oim/oim} mice, a well-studied animal model of moderate to severe OI, suggesting that disruption of a vascular SSC niche is a feature of OI pathogenesis. Moreover, crossing *Col1a2*^{oim/oim} mice to mice lacking a negative regulator of skeletal angiogenesis and bone formation, Schnurri 3 (SHN3), not only corrected the SSC and AEC phenotypes but moreover robustly corrected the bone mass and spontaneous fracture phenotypes. As this finding suggested a strong therapeutic utility of SHN3 inhibition for the treatment of OI, a bone-targeting AAV was used to mediate *Shn3* knockdown, rescuing the *Col1a2*^{oim/oim} phenotype and providing therapeutic proof-of-concept for targeting SHN3 for the treatment of OI. Overall, this work both provides proof-of-concept for inhibition of the SHN3 pathway and more broadly addressing defects in the stem/osteoprogenitor niche as is a strategy to treat OI.

Bone Research (2024)12:46

; <https://doi.org/10.1038/s41413-024-00349-1>

INTRODUCTION

Osteogenesis imperfecta (OI) is a disorder with heterogeneous genetic causes that prominently include mutations in the type I collagen genes, *COL1A1* and *COL1A2*. The hallmark of OI is low bone mass and skeletal fragility, resulting in susceptibility to fracture.^{1,2} Currently, treatments including anti-resorptive drugs bisphosphonates (e.g., alendronate and zoledronate) are used for severe OI, though their efficacy in reducing fracture rates remains under investigation.^{3–11} Bone anabolic agents, including are also under investigation for their potential benefit to OI patients in both preclinical and clinical trials.^{5,6} Experimental therapies inhibiting TGF signaling are also under study for treatment of OI.¹² Despite these advances and ongoing investigation there is still not a standard of care that has been clearly established to reduce fracture rates in OI and therefore a remaining unmet need for OI treatments. Whereas most therapeutic efforts in OI directly target well-established directly regulators of osteoblast or osteoclast activity, we hypothesized that skeletal microenvironmental dysregulation may also be a core feature of OI pathogenesis in addition to osteoblast

intrinsic defects. Thus, targeting pathways that can both rescue these microenvironmental defects and cell-intrinsic defects in osteoblast activity may provide a new and effective strategy for OI treatment.

Along these lines, it is increasingly appreciated that ancillary tissue types such as vascular endothelium present in bone actively contribute to osteogenesis.^{13,14} Though it is known that deposition of collagen type I is critical for coupling between angiogenesis and osteogenesis during skeletal development, the degree to which the vascular microenvironment of bone is dysregulated in OI is unclear.^{15,16} It is also unknown how OI disrupts the early stem and progenitor cellular compartment in bone, especially a recently identified population of cells displaying formal evidence of stemness, SSCs that are defined through multi-color flow cytometry as lineage-Thy1-6C3-alpha-v integrin⁺CD200⁺CD105⁺ cells.^{17,18}

In considering alternative approaches to augment bone formation and correct any potential vascular microenvironmental defects in OI, Schnurri-3 (SHN3, HIVEP3), a critical negative regulator of bone formation in both mice and humans offers an attractive novel

¹State Key Laboratory of Cellular Stress Biology, Cancer Research Center, School of Medicine, Faculty of Medicine and Life Sciences, Xiamen University, Xiamen 361102, China;

²Fujian Provincial Key Laboratory of Organ and Tissue Regeneration, School of Medicine, Xiamen University, Xiamen 361102, China; ³Department of Sports Medicine, Xiangya Hospital, Central South University, Changsha 410000, China; ⁴Research Division, Hospital for Special Surgery, New York, NY 10065, USA; ⁵Department of Pathology and Laboratory Medicine, Weill Cornell Medical College, New York, NY 10065, USA and ⁶Department of Electronic and Computer Engineering, Ritsumeikan University, Kusatsu, Shiga 525-8577, Japan

Correspondence: Matthew B. Greenblatt (mag3003@med.cornell.edu) or Ren Xu (xuren526@xmu.edu.cn)

These authors contributed equally: Na Li, Baohong Shi

Received: 9 July 2023 Revised: 18 June 2024 Accepted: 24 June 2024

Published online: 26 August 2024

approach.^{19,20} Mice lacking SHN3 display an osteosclerotic phenotype with profoundly augmented osteoblast activity leading to near absolute protection from age-related bone loss. In addition to the ability of SHN3 deficiency to directly drive the intrinsic bone formation activity of osteoblasts, SHN3 deficiency also acts in osteoblasts to control the skeletal vascular microenvironment by regulating production of a recently described osteoblast derived angiogenic factor, SLIT3.^{14,21} Consistent with this, SHN3 deficient mice (*Shn3*^{-/-}) mice display both enhanced bone formation and increased amounts of skeletal vascular endothelium, and both of these phenotypes are SLIT3 dependent.¹⁴ Thus, the SHN3/SLIT3 signaling axis in osteoblasts offers a potential method to not only increase bone formation but also to address microenvironmental disruption occurring in skeletal disorders.

Here we sought to determine whether skeletal microenvironmental dysfunction occurs in OI and how this may impact early SSC populations, using a widely studied OI mouse model, *Col1a2*^{oim/oim} mice (OIM mice) displaying spontaneous fractures.²² We further find evidence that correcting these defects in the skeletal vascular microenvironment can ameliorate the OI phenotype, as SHN3-deficiency can rescue the *Col1a2*^{oim/oim} model, correcting both the dysregulation in the SSC vascular niche and skeletal fragility in the *Col1a2*^{oim/oim} model.

RESULTS

Altered skeletal vascular composition in *Col1a2*^{oim/oim} mice
Though deposition of collagen type I has been suggested to mediate coupling between angiogenesis and osteogenesis during bone formation, the degree to which disruption of this osteo-angio microenvironment contributes to OI and the specific forms of vascular endothelium that are impacted remain unclear.^{14,23} To address this, we selected *Col1a2*^{oim/oim} mice as a model for human OI. As anticipated, *Col1a2*^{oim/oim} mice showed a severe osteopenic phenotype and spontaneous bone fractures relative to littermate controls in 4 weeks old (Fig. 1a, b). To avoid potential confounding due to the presence of fracture healing responses, we selected adolescent *Col1a2*^{oim/oim} mice without spontaneous fractures for further examination.

Of note, a series of recent studies revealed that skeletal endothelial cells can be further divided into two separate subpopulations, arterial endothelial cells (AECs) and sinusoidal endothelial cells (SECs), each of which plays a distinct role in the regulation of non-endothelial cells in bone through angiokine secretion.²⁴ Compared to SECs, AECs express lower levels of osteogenic factors such as SEMA3A as well as higher levels of the soluble factors inhibiting ossification such as FSTL1 (Fig. S1), indicating that they may each differ in their regulation of bone metabolism.

We then established a new multi-color flow cytometry using the combination of podoplanin (PDPN) and Sca-1 to distinguish AECs from SECs in the marrow cavity²⁵ (Fig. 1c). Based on this, the population of AECs but not SECs was significantly elevated in bones of *Col1a2*^{oim/oim} mice (Fig. 1d). Consistent with this, whole mount staining of optically cleared bone tissue further confirmed that the abundance of arterial vessels was substantially increased in the bones of *Col1a2*^{oim/oim} mice relative to those of littermate controls (Fig. 1e). Of note, this effect was specific for AECs, as other forms of skeletal endothelium, including CD31^{hi} endomucin^{hi} (EMCN^{hi}) endothelial cells²³ were not altered (Fig. S2a, b). Interestingly, the pathological extension of AECs was also observed in *Slit3*^{osx} mice, a genetic model showing a decrease in CD31^{hi} EMCN^{hi} endothelial cells as well as bone loss (Fig. S3a–c). Thus, expansion of AECs is a feature of an OI animal model.

Elevated abundance of skeletal stem cells in *Col1a2*^{oim/oim} mice
Skeletal stem cells (SSCs) serve as the ultimate source of all bone-forming osteoblasts, therefore perturbations in the SSC

compartment are likely central to many skeletal disorders.^{26,27} Considering that AECs regulate hematopoietic stem cell (HSC) proliferation,²⁵ we then considered whether the arterial EC expansion seen in OI may similarly translate to SSC alterations. To evaluate this, we utilized an established multi-color flow cytometry panel identifying SSCs¹⁸ to analyze skeletal stem/progenitor cells populations in long bones and microdissected epiphyses and metaphyses of *Col1a2*^{oim/oim} mice (Figs. 2a and S4a). Interestingly, the abundance of immunophenotypic SSCs was elevated in *Col1a2*^{oim/oim} mice, yet the amounts of pre-bone cartilage skeletal progenitors (pre-BCSPs) and bone cartilage skeletal progenitors (BCSPs), SSC-derived non-stem progenitors,¹⁷ was unchanged (Figs. 2b and S4b, c). This, alteration in the ratio of different stages of SSC maturation indicates that OI impacts the stem cell differentiation hierarchy. Consistent with this, the number of cells expressing CD200 and Sox9 markers of SSCs, but not non-stem populations expressing CD105, were increased in the resting zone of the growth plate in *Col1a2*^{oim/oim} mice, a region characterized as housing more SSCs^{16,17,28,29} (Figs. 2c and S4d). Moreover, delayed osteogenesis attributed to impaired mineralization was observed in *Col1a2*^{oim/oim} mice evidenced by the whole-mount skeletal staining in mice post 7 days of birth (Fig. 2d, e), with the early emergence of this phenotype being consistent with alterations in the early SSC compartment in addition to dysfunction of mature osteoblasts. Given increase in both SSCs and AECs seen in *Col1a2*^{oim/oim} mice, disruptions in an angiogenic SSC niche are likely contributors to the overall OI skeletal phenotype.

Col1a2^{oim/oim} SSCs lacking osteogenic capacity are highly proliferative

To gain mechanistic insight into how SSCs were influenced in *Col1a2*^{oim/oim} mice, we performed RNA-sequencing (RNA-seq) transcriptional profiling of SSCs derived from neonatal *Col1a2*^{oim/oim} mice and littermate gender-matched WT controls. SSCs from *Col1a2*^{oim/oim} mice exhibited distinctive transcriptomic features including 1 357 downregulated genes and 1 340 upregulated genes compared with SSCs from WT controls (Fig. 3a, b). By gene set enrichment analysis (GSEA), *Col1a2*^{oim/oim} SSCs displayed transcriptional features of impaired collagen synthesis capacity and impaired osteoblastogenesis, consistent to the delayed mineralization and skeletal phenotypes in *Col1a2*^{oim/oim} mice (Fig. 3c, d, upper). *Col1a2*^{oim/oim} SSCs also displayed transcriptional features consistent with an increase in mitotic rate and increased expression of SSC-related but not AEC-related genes (Fig. 3c, d, lower and Fig. S5a, b), corresponding to the elevated abundance of SSCs in *Col1a2*^{oim/oim} mice (Fig. 2a, b). Moreover, expression of genes related to early osteogenesis and endochondral ossification were also decreased in SSCs derived from *Col1a2*^{oim/oim} mice (Fig. 3e). Taken together, these findings implicate a broader set of cellular pathologies, including defects in SSCs and AECs, beyond functional defects in mature osteoblasts in OI.

Deletion of SHN3 improves bone properties in *Col1a2*^{oim/oim} mice
There remains a substantial unmet clinical need for OI treatments that reduce fracture risk in OI.^{11,30} We have previously reported that SHN3 acts as a cell-intrinsic negative regulator of both osteoblast bone formation activity and the ability of osteoblasts to promote an osteoanabolic vascular microenvironment in bone.¹⁴ Notably, the level of *Shn3* expression was elevated in bulk skeletal transcriptional analysis but not isolated SSCs from *Col1a2*^{oim/oim} mice (Figs. S5c and S6a). To understand the expression pattern of *Shn3* in skeletal cells of *Col1a2*^{oim/oim} mice, we sorted skeletal cells from bones of *Col1a2*^{oim/oim} mice and their littermates controls for single-cell RNA-sequencing (scRNA-seq). We observed an increase in *Shn3*

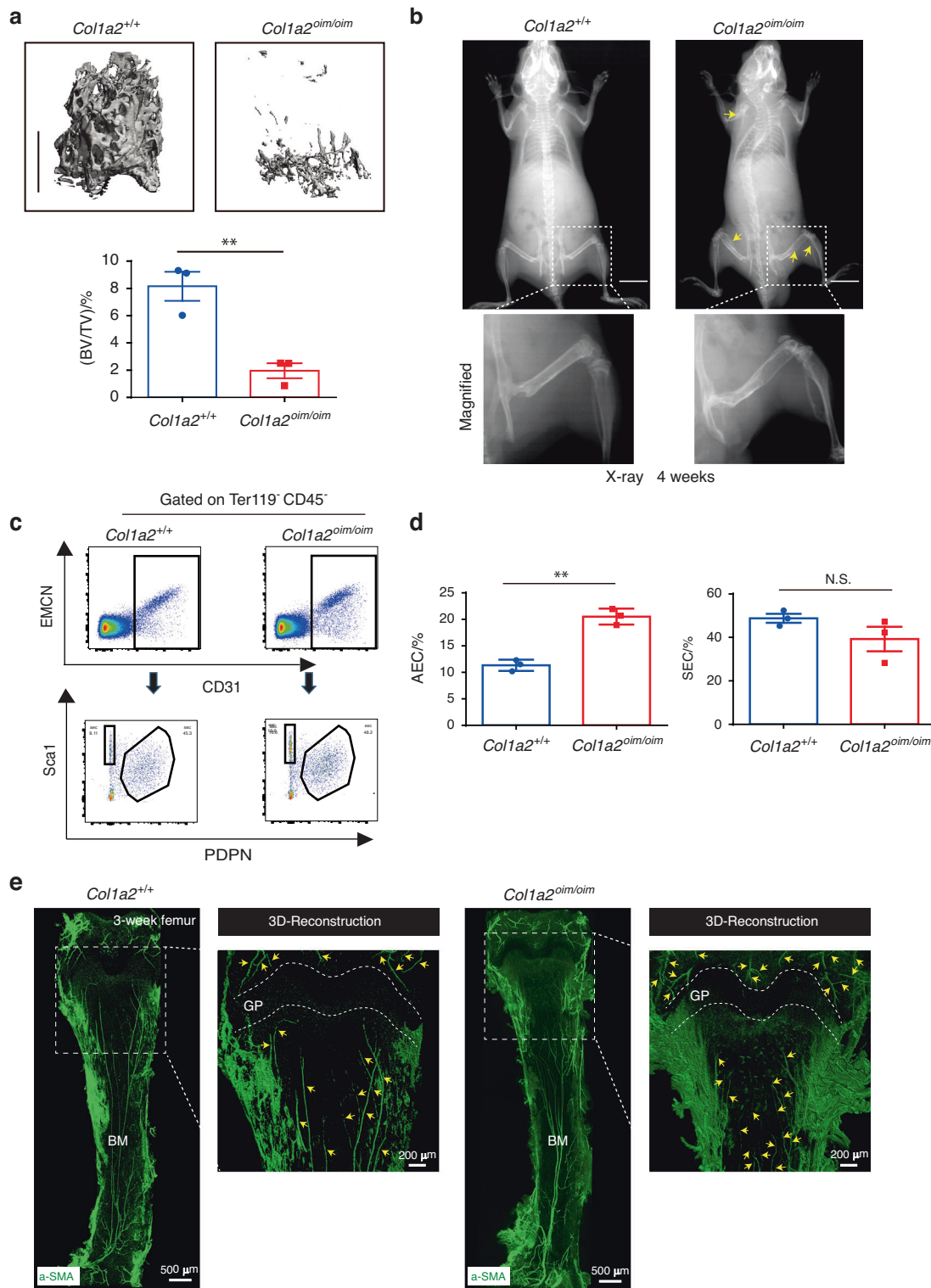


Fig. 1 Altered skeletal vascular composition in *Col1a2*^{oim/oim} mice. **a** Representative μ CT images of trabecular bone in the distal femur (left) and bone volume/total volume (BV/TV) (right) in *Col1a2*^{+/+} and *Col1a2*^{oim/oim} male mice at 6 weeks of age ($n = 3$). **b** Representative X-ray images of *Col1a2*^{+/+} and *Col1a2*^{oim/oim} male mice at 4 weeks of age. Scale bars, 1 cm ($n = 3$). **c** Representative flow cytometry plots and **(d)** quantitative analysis of arterial endothelial cells (AECs) and sinusoidal endothelial cells (SECs). Results are presented as mean \pm SEM; ** $P < 0.01$ by an unpaired two-tailed Student's t test in all panels, N.S. not significant. **e** Representative confocal images of femur tissue clearing from 3-week-old *Col1a2*^{+/+} and *Col1a2*^{oim/oim} mice stained with α -SMA (Green). Scale bars, 500 μ m

expression in preosteoblasts but not other skeletal cell populations in *Col1a2*^{oim/oim} mice (Fig. S6b–d). In addition to possibly impacting cell-intrinsic bone formation capacity of the osteolineage cells displaying increases in *Shn3* expression, increases in

Shn3 expression may also indirectly influence SSCs by reshaping the skeletal vascular niche¹⁴ (Fig. S6e).

To evaluate both whether SHN3 inhibition is a potential therapeutic approach to treat OI and also whether SHN3-

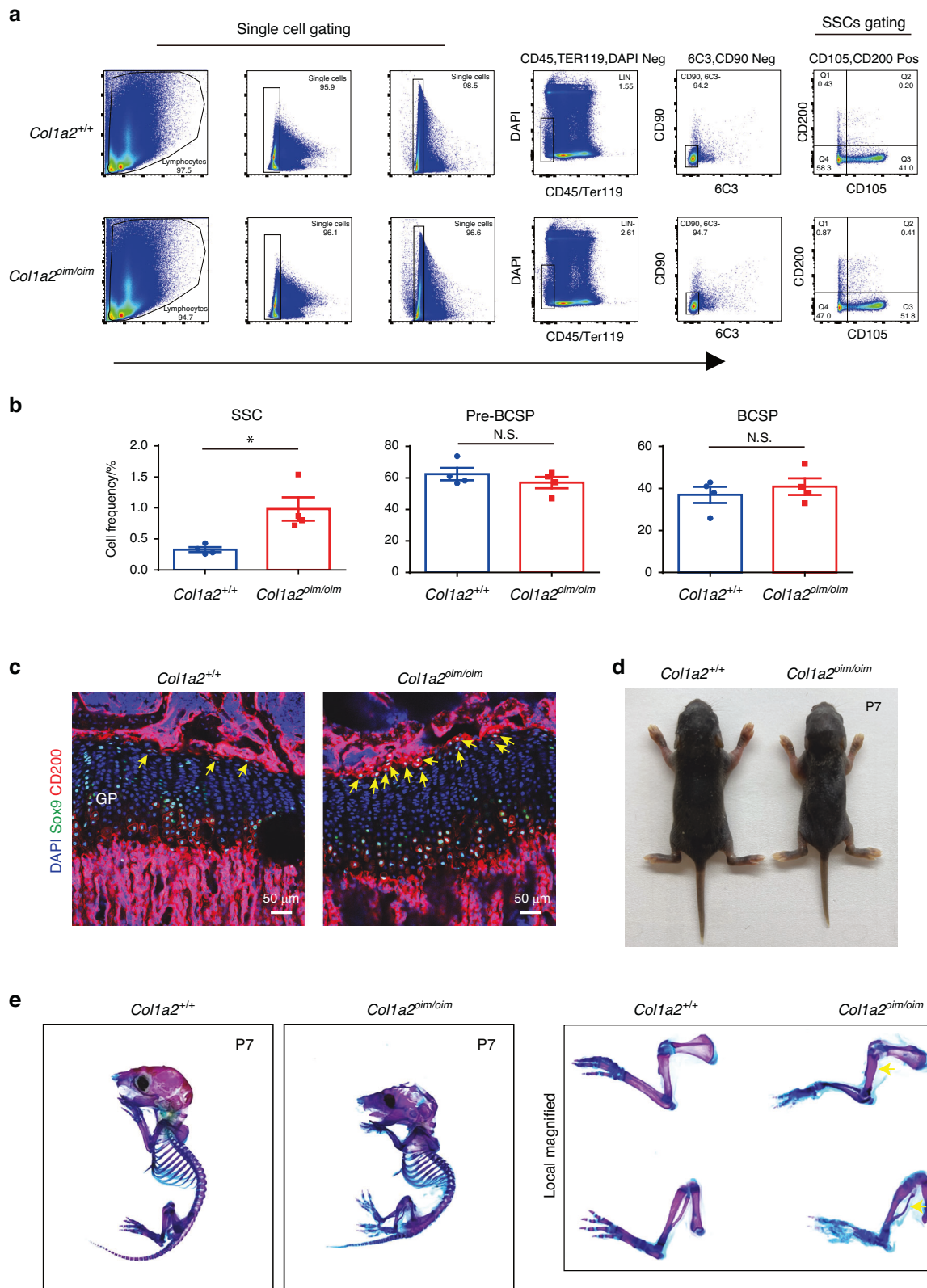


Fig. 2 Elevated abundance of skeletal stem cells in *Col1a2*^{oim/oim} mice. **a** Flow cytometry gating strategies for analysis of SSC, pre-BCSP and BCSP proportions. **b** Dot plot for analysis of SSC, pre-BCSP and BCSP proportions in *Col1a2*^{oim/oim} mice and *Col1a2*^{+/+} littermate controls. Results represented as mean ± SEM; **P* < 0.05 by an unpaired two-tailed Student's *t* test in all panels, N.S. not significant. **c** Representative confocal images (*n* = 3 total images per group) of femur sections from 3-week-old *Col1a2*^{+/+} and *Col1a2*^{oim/oim} male mice stained with CD200 (Red) Sox9 (Green) and DAPI (Blue). Scale bars, 50 μm. **d** Whole body image of *Col1a2*^{+/+} and *Col1a2*^{oim/oim} at postnatal day 7. **e** Alcian blue and alizarin red staining of skeletal preparations of newborn mice at postnatal day 7

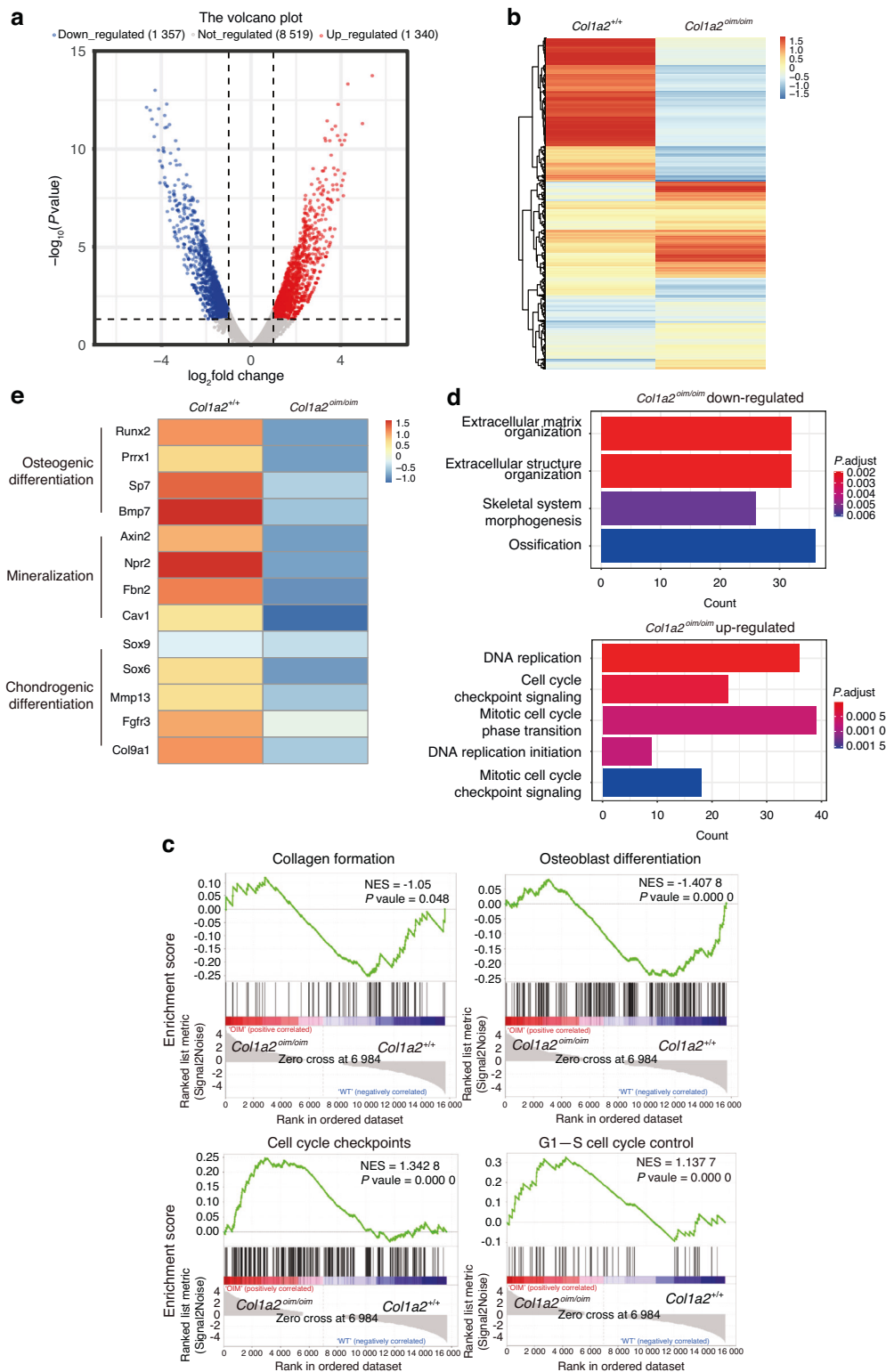


Fig. 3 *Col1a2*^{oim/oim} SSCs display cell-intrinsic transcriptional alterations and functional defects in osteogenic capacity. **a** Volcano plot illustrating differentially regulated gene expression from Bulk RNA-seq analysis between the 7-day postnatal control *Col1a2*^{+/+} mice SSCs and SSCs from the *Col1a2*^{oim/oim} mice. **b** Hierarchical clustering based on Euclidian distance using Illumina TruSeq RNA Sample Preparation kit and sequenced on Illumina HiSeq 4000. Blue, downregulated; Red, upregulated. **c** Gene set enrichment plot demonstrated activation of Collagen formation, Osteoblast differentiation, Cell cycle checkpoints and G1-S cell cycle control signaling. *Col1a2*^{+/+} and *Col1a2*^{oim/oim} represent mixture 3 biologically distinct samples. The expression pattern of genes involved in the Collagen formation, Osteoblast differentiation, cell cycle checkpoints and G1-S cell cycle control signaling set in the analysis database is shown. NES normalized enrichment score. Blue, downregulated; Red, upregulated. **d** Gene Ontology (GO) functional clustering of the interested downregulated and upregulated biological process (BP) in *Col1a2*^{oim/oim} mice SSCs. (Top, downregulated; Bottom, upregulated). **e** Heatmap for osteogenic cartilage-related gene expression in *Col1a2*^{+/+} mice SSCs (left) and *Col1a2*^{oim/oim} mice SSCs (right)

mediated regulation of the skeletal vascular microenvironment is relevant to OI phenotypes, we intercrossed *Shn3*^{-/-} mice with *Col1a2*^{oim/oim} mice.¹⁴ Ablation of SHN3^{19,31} provided a complete or near complete reversal of the low bone mass observed in both trabecular and cortical bone compartments in both male and female *Col1a2*^{oim/oim} mice (Figs. 4a–c and S7). Histomorphometric analysis revealed that SHN3-deficiency was sufficient to reverse the osteopenic phenotype and attenuated osteoblast numbers in *Col1a2*^{oim/oim} mice (Fig. 4c, d). Likewise, the decrease in bone formation rate (Fig. 4e) observed in *Col1a2*^{oim/oim} mice was normalized through additional deletion of *Shn3*. To be noted, deletion of *Shn3* in vivo increased the expression of *Slit3*, a SHN3-regulated osteoanabolic factor, to the normal level (Fig. S8a), but not altered the pathological collagen construction in the bones of *Col1a2*^{oim/oim} mice (Fig. S8b, c). However, SHN3 ablation can not significantly normalize bone length in OIM mice (Fig. S9). Thus, deletion of *Shn3* is capable to block OI-induced bone loss mainly by normalizing bone remodeling.

Ablation of *Shn3* prevents spontaneous fractures in *Col1a2*^{oim/oim} mice While it is encouraging that SHN3-deficient *Col1a2*^{oim/oim} mice display a restoration of bone formation parameters, the most clinically relevant endpoint is the prevention of fractures, the major source of morbidity in clinical OI. Indeed, *Col1a2*^{oim/oim} mice displayed spontaneous fractures starting at 3 weeks of age that increased in frequency until an average of 3 fractures per mouse could be seen at 8 weeks of age (Fig. 5a–c). Strikingly, we found SHN3 deficiency is able to completely prevent the spontaneous bone fractures in *Col1a2*^{oim/oim} mice as no fractures occurred in *Shn3*^{-/-}*Col1a2*^{oim/oim} mice. This protection from fracture in *Shn3*^{-/-}*Col1a2*^{oim/oim} mice also correlated with rescue of the running seen in *Col1a2*^{oim/oim} mice, perhaps reflecting the effect of fracture-associated stress on skeletal growth. Thus, SHN3 deficiency not only normalizes bone formation in *Col1a2*^{oim/oim} mice but completely prevents the signature spontaneous fractures occurring in this OI model.

SHN3 deficiency corrects the vascular and SSC compositional changes in *Col1a2*^{oim/oim} mice

We next evaluated whether the ability of SHN3-deficiency to rescue the spontaneous fractures in *Col1a2*^{oim/oim} mice reflected a correction of the skeletal microenvironment. To this end, we analyzed the cellular composition of the vascular endothelium and SSC compartments in *Shn3*^{-/-}*Col1a2*^{oim/oim} mice using a previously reported multi-color flow cytometry panel.¹⁷ Strikingly, *Shn3* deficiency rescued the skeletal vascular pathology in *Col1a2*^{oim/oim} mice. *Shn3*-depletion attenuated the AECs expansion seen in *Col1a2*^{oim/oim} mice while not impacting the amount of SECs and the distribution of type H vascular endothelium (Figs. 6a–d and S10). Interestingly, SHN3 deficiency alone did not notably alter the amount of SSCs or their production of downstream cell types. Consistent with this, *Shn3*-deficiency did not rescue the high proliferation of SSCs seen in *Col1a2*^{oim/oim} mice in vitro, though enhancing the late stage of osteoblast differentiation driven by SSCs (Fig. S11a, b). Despite this, *Shn3*-deficiency reversed the SSC expansion seen in *Col1a2*^{oim/oim} mice in vivo, limiting the hyperproliferative phenotype seen in the SSC-enriched region of the resting zone of the growth plate in *Col1a2*^{oim/oim} mice (Fig. 6e–h). These results implied that the expansion of SSCs is closely linked to the AECs expansion seen in *Col1a2*^{oim/oim} mice, in line with emerging evidence that endothelial cells play a critical role in the SSC niche.³² Thus, deletion of SHN3 corrected the alterations in AECs and SSC numbers seen in *Col1a2*^{oim/oim} mice (Fig. 6a, e). This finding also links correction of these cellular pathologies with overall rescue of the OI phenotype.

Shn3-silencing is a candidate therapeutic approach for OI AAV-based gene therapy is emerging as an attractive modality for the treatment of skeletal disorders due to its ability to potentially mediate long-lasting effects after a single treatment and the ability to address therapeutic targets that are challenging for traditional small molecule or biologic therapies, such as *Shn3*.^{33–35} Previous studies utilized AAV serotype-9 to deliver a *Shn3*-silencing construct that mediated a robust reduction in *Shn3* expression in osteoblastic lineage cells and accordingly augmented bone mass under both baseline physiologic conditions and in a mouse model of postmenopausal osteoporosis.³⁶ To investigate whether a gene therapy approach to inhibit SHN3 expression is capable of treating OI, we constructed replication-defective recombinant AAV serotype 9 (rAAV9) harboring enhanced green fluorescent protein (EGFP)-expressing plasmids that additionally bear either a *Shn3* targeting artificial microRNA (rAAV9-amiR-*Shn3*) or a miRNA-control (rAAV9-amiR-Ctrl) as previously described.³⁶ This vector displayed robust tropism of for osteoblasts and favorable relative specificity of payload delivery after intra-articular injection in prior studies.³⁶ We administered rAAV9-amiR-*Shn3* or rAAV9-amiR-Ctrl to *Col1a2*^{oim/oim} mice via intra-articular injection at 4 weeks of age into contralateral limbs of the same mouse and evaluated their skeletal phenotype at 12 weeks of age (Fig. 7a). Through IVIS optical imaging, expression of eGFP was predominantly localized to the hindlimb of rAAV9-injected mice, with both the femur and tibia displaying high intensity eGFP expression (Fig. 7b, c). Fluorescence microscopy confirmed that bone-lining osteoblasts were effectively transduced by the rAAV9 vector (Fig. 7d). Real-time PCR found that *Shn3* expression in femurs of OIM mice injected with rAAV9-amiR-*Shn3* decreased by 70% (Fig. 7e). Furthermore, trabecular bone volume was significantly higher in rAAV9-amiR-*Shn3* administered limbs compared to contralateral rAAV9-amiR-Ctrl limbs and cortical bone is also significantly thickened, which reduces the probability of fractures (Fig. 7f, g). Bone tissue clearing further showed that the number of arterioles was reduced in *Col1a2*^{oim/oim} mice after rAAV9-amiR-*Shn3* treatment (Fig. 7h); meanwhile, the pathological expansion of growth plate SSCs seen in *Col1a2*^{oim/oim} mice was ameliorated (Fig. 7i, j). This provides proof-of-concept that postnatal therapeutic targeting of *Shn3* is able to reverse the osteopenia seen in the *Col1a2*^{oim/oim} mice and provides specific demonstration of an AAV-based gene therapy approach to *Shn3* targeting.

DISCUSSION

Currently, there remains a substantial unmet clinical need for methods to treat OI, as it remains an area of active investigation whether anti-resorptive drugs such as bisphosphonates or other repurposed osteoporosis therapies will correct the increased fracture rate that is the signature clinical issue of OI. In part this unmet need is a call for both an improved mechanistic understanding of OI and for investigation into innovative means to correct or compensate for the cellular, architectural and bone materials properties deficits driving skeletal fragility in OI.

Recent advances in single-cell transcriptome analysis and the FACS-based definition of skeletal cell types have created new avenues for understanding the cellular pathogenesis of OI and other skeletal disorders, by allowing the first molecular definitions of the skeletal and endothelial cell populations comprising bone. Here we have made one of the first applications of these approaches to define alterations in skeletal cell types to a specific skeletal disease,³⁷ finding that the amount of SSCs and skeletal AECs are both significantly elevated in bones of *Col1a2*^{oim/oim} mice. Moreover, correction of the OI phenotype leads to a reversal this expansion in SSCs and AECs, arguing that this expansion is linked to OI pathogenesis. While it was well established that functional defects in mature osteoblasts are central to the pathogenesis of OI, it was unclear if there was a broader dysfunction in SSCs.³⁸ Here, we first found that the amount of

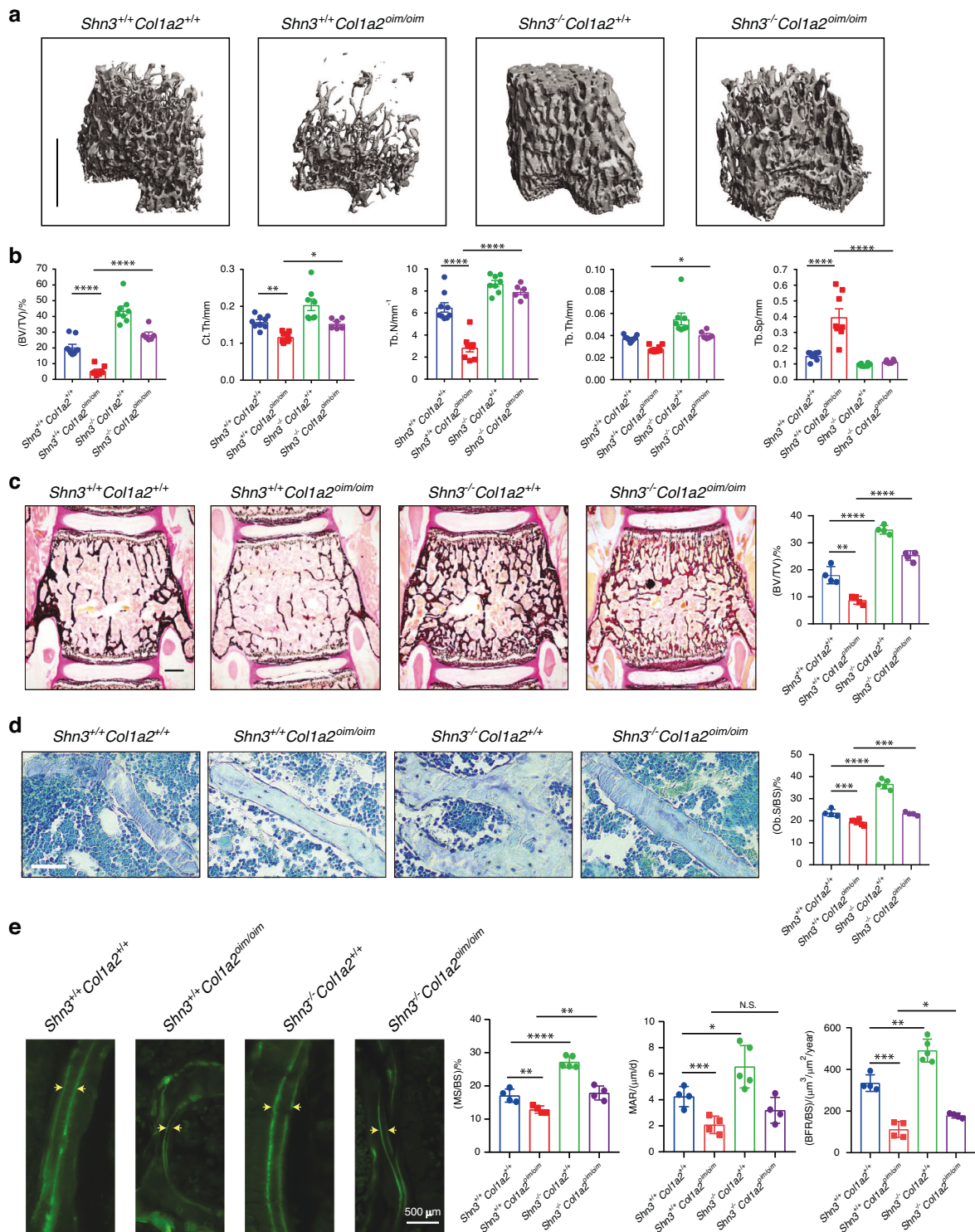


Fig. 4 Deletion of SHN3 improves bone properties in *Col1a2*^{oim/oim} mice. **a** Representative μ CT images of the trabecular bone in the distal femur metaphysis and **(b)** relative quantitative analysis of BV/TV in *Shn3*^{+/+} *Col1a2*^{+/+} and *Shn3*^{+/+} *Col1a2*^{oim/oim} and *Shn3*^{-/-} *Col1a2*^{+/+} and *Shn3*^{-/-} *Col1a2*^{oim/oim} male mice. Analysis at 6 weeks of age. Scale bars, 1 mm. Values were presented as mean \pm SEM; * P < 0.05, ** P < 0.01 and **** P < 0.0001 by an unpaired two-tailed Student's *t* test in all panels. **c** Representative images and BV/TV analysis of Von Kossa staining and the quantification of histomorphometric parameters of L3 vertebrae in *Shn3*^{+/+} *Col1a2*^{+/+} and *Shn3*^{+/+} *Col1a2*^{oim/oim} and *Shn3*^{-/-} *Col1a2*^{+/+} and *Shn3*^{-/-} *Col1a2*^{oim/oim} male mice at 6 weeks of age. Scale bars, 500 μ m (n = 4 for each group). **d** Representative histological images of the L3 vertebrae with Toluidine blue staining and the quantification of histomorphometric parameters in *Shn3*^{+/+} *Col1a2*^{+/+} and *Shn3*^{+/+} *Col1a2*^{oim/oim} and *Shn3*^{-/-} *Col1a2*^{+/+} and *Shn3*^{-/-} *Col1a2*^{oim/oim} male mice at 6 weeks of age. Trabecular osteoblast surface/bone surface [(Ob.S/BS)/%] are shown. Scale bars, 50 μ m. *Shn3*^{+/+} *Col1a2*^{+/+} (n = 4), *Shn3*^{+/+} *Col1a2*^{oim/oim} (n = 5), *Shn3*^{-/-} *Col1a2*^{+/+} (n = 5), *Shn3*^{-/-} *Col1a2*^{oim/oim} (n = 4). **e** Representative images of calcein double labeling and quantification of histomorphometric parameters of the L3 vertebrae in *Shn3*^{+/+} *Col1a2*^{+/+} and *Shn3*^{+/+} *Col1a2*^{oim/oim} and *Shn3*^{-/-} *Col1a2*^{+/+} and *Shn3*^{-/-} *Col1a2*^{oim/oim} male mice at 6 weeks of age. Trabecular mineralizing surface/bone surface [(MS/BS)/%] mineral apposition rate [MAR]/(μ m/d), bone formation rate/bone surface [(BFR/BS)]/(μ m³/ μ m²/year) are shown. Scale bars, 100 μ m. *Shn3*^{+/+} *Col1a2*^{+/+} (n = 3), *Shn3*^{+/+} *Col1a2*^{oim/oim} (n = 4), *Shn3*^{-/-} *Col1a2*^{+/+} (n = 4), *Shn3*^{-/-} *Col1a2*^{oim/oim} (n = 4)

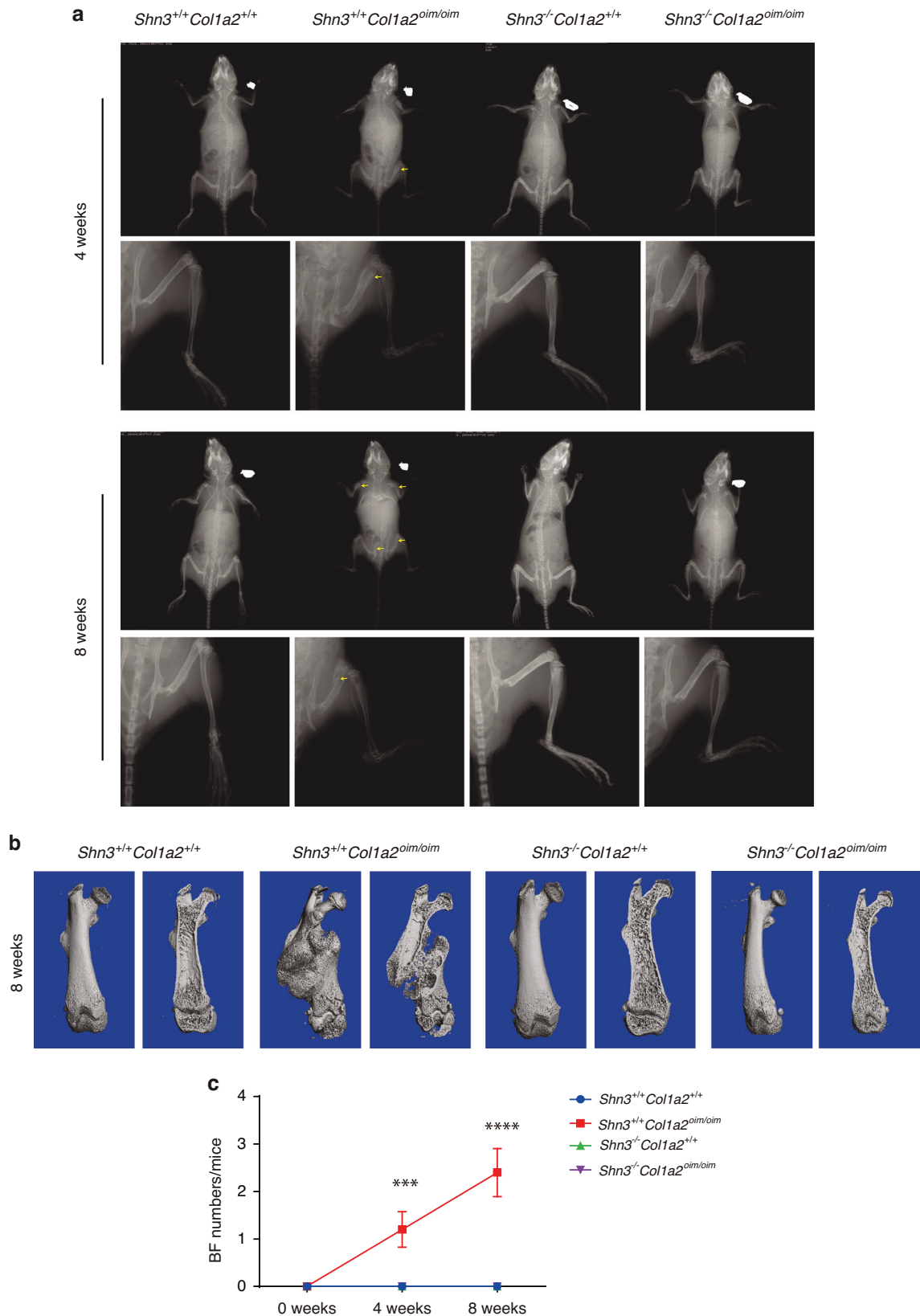


Fig. 5 Ablation of SHN3 prevents spontaneous fractures in *Col1a2^{oim/oim}* mice. **a** Representative X-ray image of *Shn3^{+/+} Col1a2^{+/+}* and *Shn3^{+/+} Col1a2^{oim/oim}* and *Shn3^{-/-} Col1a2^{+/+}* and *Shn3^{-/-} Col1a2^{oim/oim}* male mice at 4 and 8 weeks age. Scale bar: 2 mm. **b** Reconstruction of μ CT data reflected spontaneous bone fracture in *Shn3^{+/+} Col1a2^{+/+}* and *Shn3^{+/+} Col1a2^{oim/oim}* and *Shn3^{-/-} Col1a2^{+/+}* and *Shn3^{-/-} Col1a2^{oim/oim}* male mice at 8 weeks age. **c** Relative quantification of spontaneous bone fracture numbers in *Shn3^{+/+} Col1a2^{+/+}* and *Shn3^{+/+} Col1a2^{oim/oim}* and *Shn3^{-/-} Col1a2^{+/+}* and *Shn3^{-/-} Col1a2^{oim/oim}* male mice after the birth of 1 weeks. Analysis at 1, 5 and 9 weeks of age. Values represent mean \pm SEM; ** P < 0.01 and *** P < 0.001 by an unpaired two-tailed Student's t test in all panels

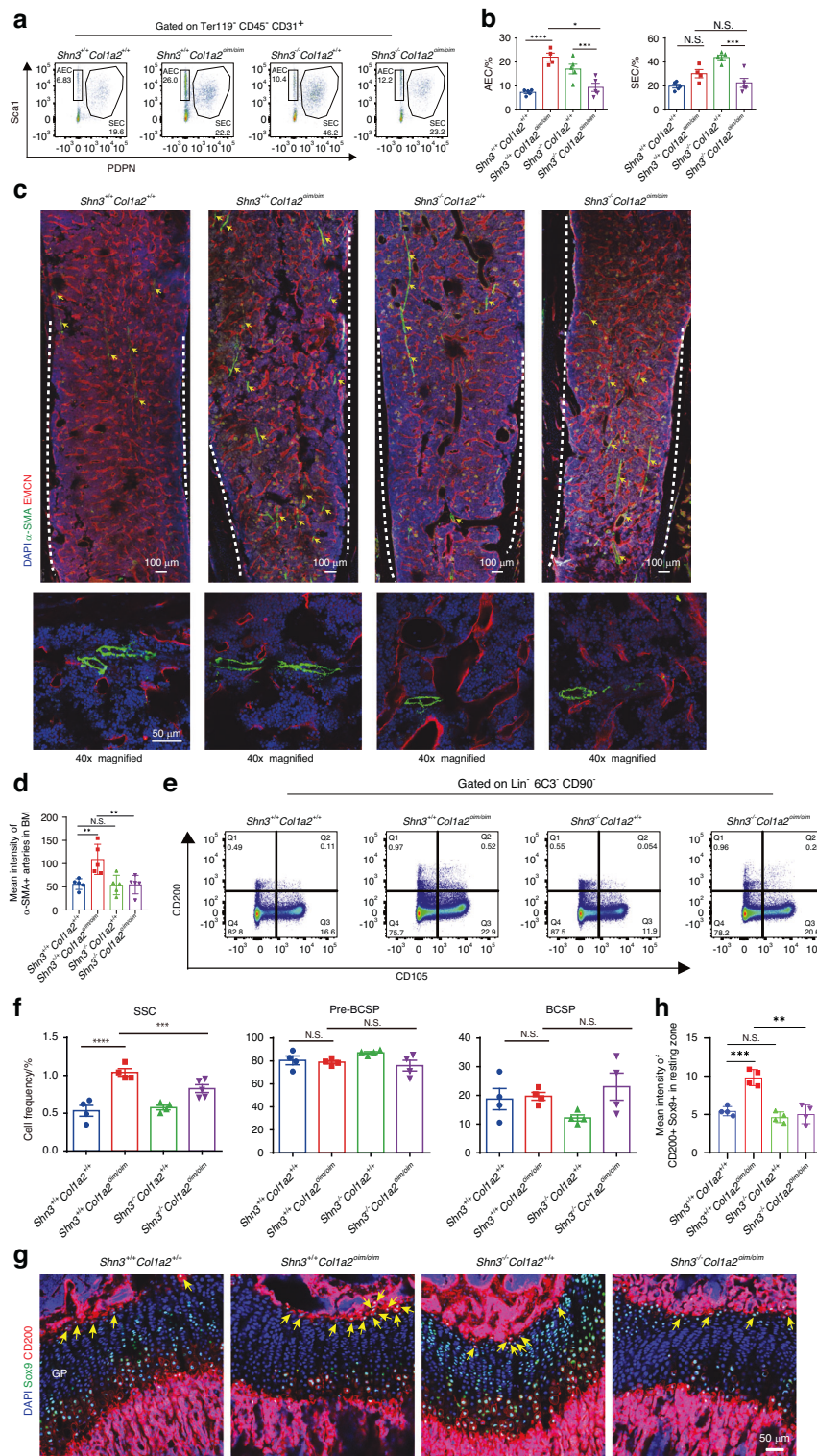


Fig. 6 SHN3 deficiency corrects abnormal vascular and SSC composition in *Col1a2^{oim/oim}* mice. **a** Experimental strategy and representative flow cytometry plots (**b**) and relative frequency of arterial endothelial cells (AECs) and sinusoidal endothelial cells (SECs). **c** Representative confocal images ($n = 3$ total images per group) of femur sections from 3-week-old *Shn3^{+/+}Col1a2^{+/+}* and *Shn3^{+/+}Col1a2^{oim/oim}* and *Shn3^{-/-}Col1a2^{+/+}* and *Shn3^{-/-}Col1a2^{oim/oim}* male mice stained with EMCN (Red) and α -SMA (Green), DAPI (Blue). Arrows show significant differences area in bone marrow. (Top, lower power; Bottom, higher power). Scale bars, 100 μ m (low power) and 50 μ m (high power). **d** Quantification of α -SMA positive cells in femur bone marrow. ($n = 5$; data are presented as means \pm SEM, P values, two-tailed unpaired t -test). **e** Experimental strategy and representative flow cytometry plots (**f**) and relative frequency of SSCs, Pre-BCSP, BCSP. **g** Representative confocal images ($n = 3$ total images per group) of femur sections from 3-week-old *Shn3^{+/+}Col1a2^{+/+}* and *Shn3^{+/+}Col1a2^{oim/oim}* and *Shn3^{-/-}Col1a2^{+/+}* and *Shn3^{-/-}Col1a2^{oim/oim}* male mice stained with antibodies recognizing Sox9 (Green), CD200 (Red) and DAPI (Blue). Scale bars, 50 μ m. **h** Quantification of CD200⁺ Sox9⁺ in resting zone of distal-femur growth plates. ($n = 3$; data are presented as means \pm SEM, P values, two-tailed unpaired t -test)

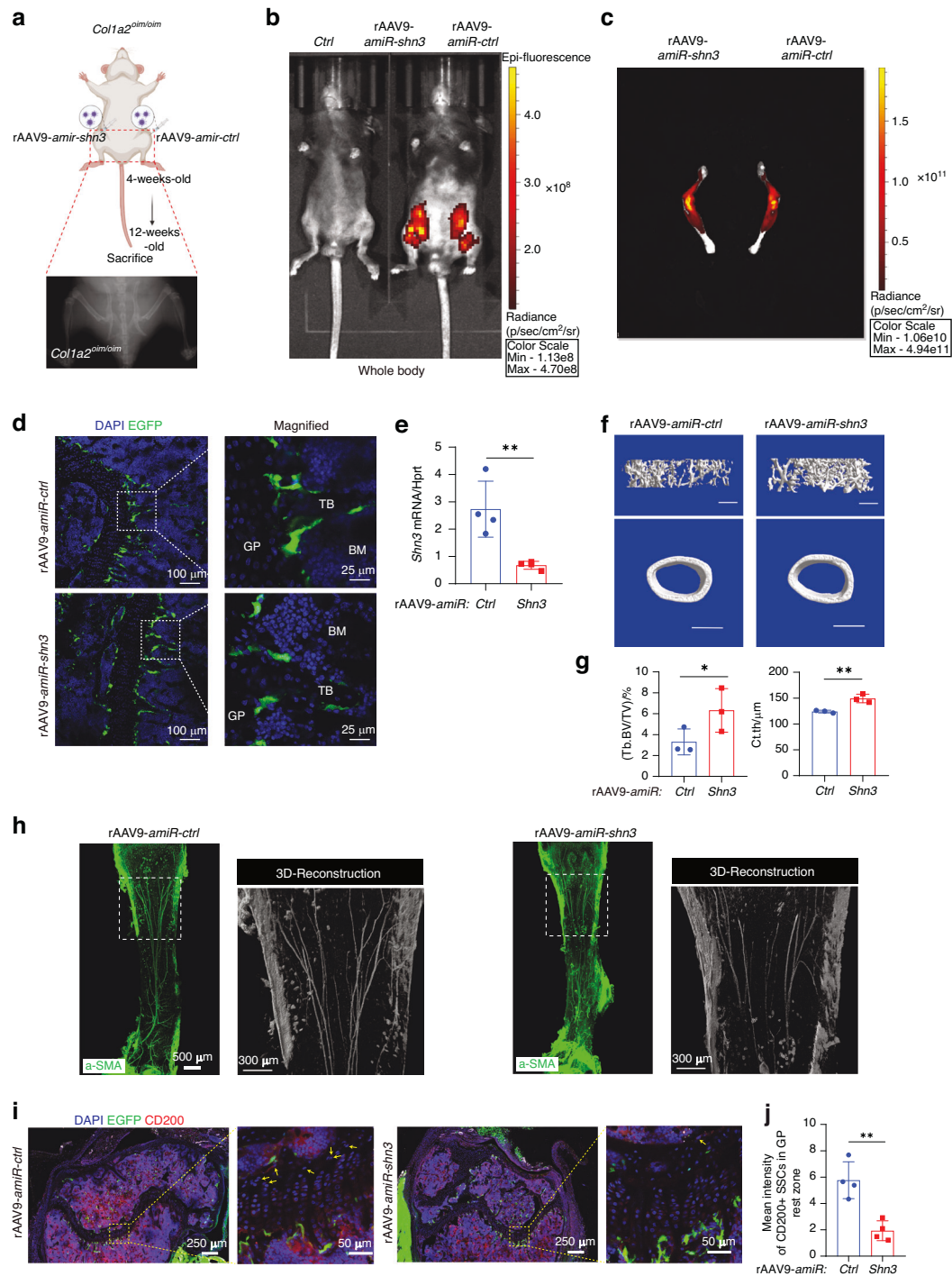


Fig. 7 SHN3-silencing is a candidate therapeutic approach for OI. **a** Schematic diagram of strategy for rAAV9-*amiR-ctrl* or *amiR-shn3* injected into knee joints in 4 weeks old *Col1a2^{oim/oim}*, rAAV9-*amiR-ctrl* in the left hindlimbs and *amiR-shn3* in the right hindlimbs, sacrificed in 12 weeks old. **b, c** Two months after i.a. injection of rAAV9 carrying *amiR-ctrl* or *amiR-shn3* into knee joints of 1-month-old male mice, EGFP expression was assessed by IVIS Lumina III optical imaging. **d** Two months after i.a. injection of rAAV9 carrying *amiR-ctrl* or *amiR-shn3* into knee joints of 1-month-old male mice, the vector-driven EGFP signal in trabecular bone was visualized by fluorescence microscopy of cryo-sectioned femurs. **e** Two months after i.a. injection of rAAV9 carrying *amiR-ctrl* or *amiR-shn3* into knee joints of 1-month-old male mice, *Shn3* mRNAs normalized to *hprt* were assessed in femur bone was assessed by real-time PCR. **f** Two months after i.a. injection of rAAV9 carrying *amiR-ctrl* or *amiR-shn3* into knee joints of 1-month-old male mice, femoral trabecular bone mass was assessed by μCT. **g** Representative 3D reconstruction and relative quantification are displayed ($n = 3$ per group), Scale bars, 100 μm. **h** Two months after i.a. injection of rAAV9 carrying *amiR-ctrl* or *amiR-shn3* into knee joints of 1-month-old male mice, representative confocal images of femur tissue clearing from 3 month-old *Col1a2^{+/+}* and *Col1a2^{oim/oim}* mice stained with α-SMA (Green). Scale bars, 500 μm. **i** Two months after i.a. injection of rAAV9 carrying *amiR-ctrl* or *amiR-shn3* into knee joints of 1-month-old male mice, the vector-driven EGFP signal in trabecular bone was visualized by fluorescence microscopy of cryo-sectioned femurs. Cryo-sectioned femurs were also immunostained with CD200 (Red) and DAPI (Blue). **j** Quantification of CD200 positive cells in resting zone of distal-femur growth plates. Right panels show magnified area of central growth plates. ($n = 4$; data are presented as means ± SEM, P values, two-tailed unpaired t -test)

SSCs were elevated in the *Col1a2^{oim/oim}* OI model, implicating altered stem cell dynamics in OI. Importantly, while the OIM model is a widely utilized and relatively severe OI model, it is driven by a mutation not known to occur in OI patients³⁹. Therefore, both due to this reason and due to the intrinsic genetic and phenotypic heterogeneity of OI, repetition of these findings across many OI models will be a valuable in establishing whether these results are broadly representative of OI pathophysiology.

The functional and physical coupling between osteogenesis and angiogenesis is increasingly emerging as a critical point of dysfunction in skeletal disorders and also a promising but largely unexplored therapeutic opportunity. Previously, we found that SHN3 acts in osteoblasts to regulate production of SLIT3, which in turn acts as a skeletal specific angiogenic factor.¹⁴ Through this angiogenic activity, SLIT3 in turn creates a skeletal vascular microenvironment that enables anabolic bone formation. We here find a linkage between AECs abundance and SSC expansion in OI that in turn suggests a broader functional linkage between AECs and SSCs, perhaps with AECs serving as part of the SSC niche. This fits with an emerging picture that specific skeletal progenitor populations may be specifically localized to perivascular or periarteriolar regions, and provides some of the first direct evidence that vascular modulation produces corresponding changes in SSCs as functional evidence for a perivascular SSC niche.^{32,40,41} This also raises the question of whether SLIT3 is a specific regulator of SSC abundance through a selective ability to modulate AECs as opposed to SECs, suggesting a model whereby the composition of skeletal vascular endothelium can be tuned by a series of subset vessel-type specific angiogenic factors, possibly including PDGF-bb, VEGF isoforms or others, that in turn govern the composition of the pool of early skeletal progenitors.⁴² In this manner, a vascular targeted osteoanabolic agent may be synergistic with a traditional osteoblast targeted osteoanabolic through activity to “prime” the osteoanabolic effect both by preparing the pool of early vasculature associated stem and progenitor cells and also by creating a microenvironment that favors bone formation. Thus, the SHN3-targeting gene therapy approach taken here is also anticipated to be complementary to either established osteoanabolic or anti-resorptive therapeutics or to emerging therapeutic approaches that specifically target the molecular pathogenesis of OI, such as anti TGF- β antibodies.^{5,12}

Whether achieved via a gene therapy-based approach as tested here or via other methods, inhibition of SHN3 is an attractive approach for treating OI. Prior mechanistic studies have shown that, in addition to the above ability of SHN3 to regulate the bone vascular microenvironment through regulation of SLIT3 secretion, SHN3 mediates a cell-intrinsic effect in osteoblasts to suppress bone formation. This occurs in part via the ability of SHN3 to suppress ERK-mediated phosphorylation of selected substrates.^{19,31} While SHN3 is broadly expressed, the phenotypes associated with SHN3 deficiency appear to be limited to the skeleton, which is promising for the possibility that SHN3-targeted therapies will display a favorable effect to toxicity profile.

In summary, this project has identified new cellular features of OI in the SSC and vascular compartments of bone and identified preclinical evidence supporting a new therapeutic approach centering on inhibition of the SHN3 pathway with an AAV delivered payload. We anticipate that this will not only motivate further development of AAV and SHN3-based gene therapeutic approaches, but moreover provide evidence for marked disruption in the vascular and SSC compartments as a feature of OI that could be central to disease pathogenesis.

MATERIALS AND METHODS

Animals

Col1a2^{oim/oim} mice were obtained from the Jaxson Laboratory (B6C3Fe a/a-*Col1a2^{oim}*/J, Stock No: 001815, Bar Harbor, ME, USA);

Shn3^{-/-} mice were described in our previous studies.^{14,19} Dual heterozygous *Shn3^{+/-}Col1a2^{oim/+}* mice were used for breeding to generate *Shn3^{+/+}Col1a2^{+/+}* mice, *Shn3^{+/+}Col1a2^{oim/oim}* mice, *Shn3^{-/-}Col1a2^{+/+}* mice and *Shn3^{-/-}Col1a2^{oim/oim}* mice. All mice were housed up to four per cage under a 12-h light-dark cycle with chow ad libitum in the Laboratory Animal Center at the Xiamen University. All mouse experiments were handled according to the protocols approved by the Institutional Animal Care and Use Committee of Xiamen University Laboratory Animal Center.

Radiography and micro-CT analysis

Whole-body radiographs of experimental mice were captured by a Faxitron X-ray system. We defined fractures in the humerus, forearms, femurs and tibias by bone deformity and callus formation. We performed μ CT scanning using a μ CT 35 system (Scanco Medical, Sweden) at the Weill Cornell-Citigroup Biomedical Imaging Core according to the parameters in our previous study.²¹ The analysis was conducted by a technician blinded to the genotypes of the mice under analysis.

Histology and dynamic histomorphometry

We injected the experimental and control mice intraperitoneally with a dose of 20 mg/kg calcein on days 1 and 5 before sacrifice for measurement of bone formation rate. Resin embedding and sectioning without decalcification was performed for von Kossa staining and toluidine blue staining as described in our previous study.⁴³ We then use the Osteomeasure System (OsteoMetrics, Atlanta, USA) for histomorphometric analysis as previously described.¹³

Immunofluorescence staining

Frozen sectioning for skeletal immunofluorescence staining were prepared according to a published protocol and our recent studies.^{14,18,44} Primary antibodies (rat anti-mouse CD200 (Abcam), rabbit anti-mouse SP7 (Abcam, USA), goat anti-mouse CD31 (R&D, USA), rat anti-mouse endomucin (Santa Cruz, USA), rabbit anti-mouse α -SMA (Proteintech, China), rabbit anti-mouse Sox9 (Abcam, USA) and rabbit anti-mouse CD105 (Abcam, USA) and species-specific secondary antibodies with Alexa Fluor 488 and 594 (Invitrogen, USA) were used in this study.

Bone tissue 3D imaging

The iDISCO method was utilized as published.^{45,46} In brief, 3-week *Col1a2^{+/+}* and *Col1a2^{oim/oim}* mice or 3-month *Col1a2^{oim/oim}* mice femurs were decalcified in 350 mmol/L EDTA-Na (pH6.5) at 37 °C for 72 h, with buffer changes every 24 h. Fixed femurs were washed in 20%, 40%, 60% and 80% methanol in H₂O, and then 100% methanol. Femurs were incubated in 100% methanol overnight at 4 °C, and then washed in 80%, 60%, 40%, and 20% methanol in H₂O. Femurs were then washed in PBS/0.1% Triton X-100/0.05% Tween-20/2 mg/mL heparin for three 1 h washes, then overnight. Intact femurs were incubated with the primary antibody (α -SMA, Proteintech, China) at 37 °C for 4 days in 10% DMSO/0.2% PBST (1:500 dilution). Excess antibody was washed away with 0.2% PBST at 37 °C with shaking twice for 2 h then overnight twice. Tissues were further immunolabeled with an Alexa Fluor-conjugated secondary antibody (Thermo Fisher Scientific) diluted (1:500) in 10% DMSO/0.2% PBST at 37 °C for 72 h. Excess antibody was washed away with 0.2% PBST at 37 °C with shaking for two 2 h wash sessions then overnight. Femurs were incubated at room temperature in a gradient of 20%, 40%, 60%, and 80% methanol in H₂O, and lastly 100% methanol. Femurs were then incubated at room temperature followed by a mixture of dichloromethane and methanol (v:v = 2:1) for 2 h twice, followed by 100% dichloromethane for 30 min four times. Femurs were cleared at room temperature with 100% dibenzyl-ether for 12 h three times.

Optically-cleared femurs were imaged on a Zeiss 780 Confocal Microscope equipped with a 10x/NA 0.45 Plan Apo objective. Each tissue was placed between two coverslips and imaged with a step size of 2 μm .

Flow cytometry analysis and cell sorting

To analyze skeletal endothelial cells, 3 μg PE-anti-mouse PDPN (Biolegend, USA) were injected intravenously. After 10 min, femurs were isolated from mutant mice and littermate controls and were crushed in Hank's balanced salt solution with 10 mmol/L HEPES. For the enzymatic digestion, 2.5 mg/mL Collagenase A and 1 U/mL Dispase II were added for a 15 min incubation at 37 $^{\circ}\text{C}$ with gentle agitation. Next, PBS containing 2% FBS and 2 mmol/L EDTA were added to stop the digestion, and the resulting suspension was filtered through a 70 μm cell strainer and washed twice with PBS. After blocking nonspecific staining with an anti-mouse CD16/CD32 antibody (BD Biosciences, USA) for 15 min on ice, the cells were stained with Alexa Fluor 700-conjugated Ter119 antibody (BD), Alexa Fluor 700-conjugated CD45 antibody (BD Biosciences, USA), FITC-conjugated CD31 (BioLegend, USA) and APC-conjugated EMCN antibody (eBioscience, USA). For skeletal stem cell analysis, the cells were stained with a FITC-conjugated CD45 antibody (BioLegend, USA), APC/Cy7-conjugated Ter119 antibody (BioLegend, USA), PE-conjugated CD31 antibody (eBioscience, USA), PerCP-Cy5.5-conjugated 6C3 antibody (BioLegend, USA), BV605-conjugated CD90.2 antibody (BioLegend, USA) BV421-conjugated CD200 antibody (BD Biosciences, USA) and PE/Cy7-conjugated CD105 antibody (BioLegend, USA) for 30 min on ice. One $\mu\text{g}/\text{mL}$ DAPI solution (BD Biosciences, USA) was used for live/dead exclusion with combination of FSC and SSC. Cell sorting was performed with FACS Aria II (BD, San Jose, CA, USA) and analyzed using FlowJo software (Tree Star, Ashland, OR, USA).

Bulk RNA sequencing

Bulk RNA sequencing was performed on SSCs isolated from 7-day postnatal *Col1a2^{oim/oim}* mice and littermate gender-matched controls as previously described.¹⁸ In brief, cDNA libraries were generated with the Illumina TruSeq RNA Sample Preparation kit and sequenced on an Illumina HiSeq 4000. HISAT2(v2.2.1) was used to align raw sequencing reads to the mm10 mouse reference genome. Differential expression analysis was performed using edgeR package (v 3.36.0, Bioconductor). Genes with expression level lower than 1 CPM (counts per million) were considered as displaying low expression and were excluded. The heatmap and volcano plot were generated to visualize differential genes utilizing pheatmap(v1.0.12) and ggplot2 package(v3.3.6), respectively. For gene functional annotation analysis, GO and pathway enrichment analysis was performed for upregulated/downregulated DEGs using clusterProfiler package(v4.4.4), and the *P* values of enriched terms were adjusted by Benjamini-Hochberg method and terms were filtered by setting *p*valueCutoff to 0.05. Gene set enrichment analysis was performed using the GSEA software(v4.3.2) for linux. We selected gene sets of ontology and curated signaling pathways from the MSigDB Database(v2022.1, <https://www.gsea-msigdb.org>) to identify differential gene ontology and pathways enriched in *Col1a2^{oim/oim}* and littermate mice sample subsets.

Single-cell RNA-seq

Processing of single-cell RNA-seq data was performed in Cell Ranger (version 7.0.1) for handling paired-end sequencing reads, mapping reads to the mouse genome (mm10), and generating expression matrices. Post-processing, data was analyzed using Seurat (version 5.0.2) where cells with low-quality metrics, characterized by fewer than 200 genes per cell, fewer than 3 cells per gene, Unique Molecular Identifiers (UMIs) per cell ranging from less than 500, a mitochondrial gene composition exceeding 20%, and doublets identified by DoubletFinder (version 2.0) were all excluded. Data normalization was performed using the

sctransform method, followed by PCA and clustering with the Louvain method, utilizing Uniform Manifold Approximation and Projection (UMAP) for visualization. Marker genes were identified using a Wilcoxon rank sum test, and the FindMarkers function was utilized to identify differentially expressed genes across clusters. Dot plot was employed to annotate cell subpopulations using marker genes. The expression differences in *Hivep3* expression gene between osteogenesis imperfecta (OIM) and wild-type (WT) mice was visualized using the FeaturePlot function. Additionally, Gene Ontology (GO) enrichment analysis within the preosteoblast clusters of OIM and WT mice was performed using the clusterProfiler package and visualized with the barplot package.

rAAV9-mediated silencing of *Shn3*, intra-articular injection

Artificial miRNA-containing plasmids targeting murine *Shn3* were generous gifts from Dr. Guangping Gao. Replication-deficient recombinant AAV (rAAV) vector design and production were performed as previously described.³⁶ In brief, engineered amiR cassettes targeting *Shn3* (*amiR-Shn3*) or control (*amiR-ctrl*) were constructed within vector plasmids between *CB* promoter and the reporter gene *Egfp* which enable visual tracking of transduced cells, or tissues. Plasmids containing amiR cassettes, AAV2/9 and helper plasmids were mixed and transfected into HEK293 cells using PEI-MAX 40000 (Polysciences, 24765-1) to generate rAAV for experimental use. These rAAV batches were then collected and purified following a traditional CsCl sedimentation protocol. The concentration of rAAV9-*amiR-Shn3* and rAAV9-*amiR-ctrl* was then tittered as previously described.³⁶

For local delivery of rAAV, intra-articular injections were performed when male- *Col1a2^{oim/oim}* mice or controls reached 1 month of age. To avoid confounding due to active fracture repair, *Col1a2^{oim/oim}* mice display radiographic evidence of fracture were excluded from the experimental cohort. After anesthesia and surgical site preparation, a 1-mm anterolateral skin incision was made above knee articular capsule. A total volume of 5 μL containing 1×10^{12} GC rAAV9-*amiR-shn3* or rAAV9-*amiR-ctrl* were injected into the articular capsule of contralateral hindlimb stifle/knee joints on the same host to allow for paired analysis of local effects in the same host. The needle was retained in the injection site for 2–5 min to avoid leakage. Incisions were then sutured and analgesic administration was performed as described previously.¹⁴ Eight weeks after injection, individuals were subjected to in vivo IVIS optical imaging and lower limbs were dissected for downstream analysis.

SSCs culture and differentiation assays

Femoral SSCs were sorted from 3 week old *Col1a2^{oim/oim}* mice and littermate controls by triple collagenase/Dispase II digestion. Cells were cultured in α -MEM medium (Gibco) containing 10% FBS, 2 mmol/L L-glutamine, 1% penicillin/streptomycin, 1% HEPES and 1% non-essential amino acids. Ascorbic acid (50 $\mu\text{g}/\text{mL}$) and β -glycerophosphate (5 mmol/L) were added to the culture medium for osteogenic differentiation studies, with a total of 14 days of differentiation allowed. Alizarin red staining was used to assess the ossification activity. For Alizarin red staining, cells were fixed with 4% neutral-buffered formalin for 30 min and then incubated with 2% Alizarin red S for 2 min at room temperature.

For SSC colony forming assays, 200 cells were plated into each well of a 6-well plate and cultured for 2 weeks. Cultured cells were then visualized by phase microscopy. Cells were stained with crystal violet and observed later.

Quantitative real-time PCR analysis

Total bone tissue RNA was extracted using TRIzol (Vazyme, R401-01-AA) and reverse transcription was performed with the PrimeScriptTM RT Kit (TaKaRa, Perfect Real Time) cDNA Reverse Transcription Kit from Applied Biosystems according to the

Table 1. Primer sequences for qRT-PCR

Gene	Forward	Reverse
<i>Hivep3</i>	CTGGTCCATCCAACCTCCGAA	CCTCTCTTGAAGTGGGAGTAC
<i>Slit3</i>	TCCAGTGTCTCTGAAGGCTCT	TGGCAATGCCAGGCTCCTGTGA
<i>Col1a1</i>	CCTCAGGGTATTGCTGGACAAC	CAGAAGGACCTGTTTGCCAGG
<i>Col1a2</i>	TTCTGTGGGCTCTGCTGGGAA	TTGTCACCTCGGATGCCTTGAG

manufacturer's instructions. We performed quantitative analysis of gene expression using SYBR Green PCR Master Mix (Vazyme) with a QuantStudio™ real-time PCR Instrument (Thermo Fisher Scientific, 96-Well 0.2 mL Block). *Hprt* expression was used as an internal control. The $2^{-\Delta\Delta CT}$ method was used to normalize the data. The specific primers with SYBR Green (based on the mouse sequences) are listed in Table 1.

Statistical analysis

All statistical analysis was performed using GraphPad Prism (v6.0a; GraphPad, La Jolla, CA, USA). A two-tailed Student's *t* test was used to determine significance for comparison of only two groups. One-way ANOVA with Tukey's post hoc tests were used to determine significance for comparisons between multiple groups. A *P* value < 0.05 indicated statistical significance. Error bars are presented as mean ± SEM.

ACKNOWLEDGEMENTS

We would like to thank Dr. Guangping Gao and Dr. Jae-Hyuck Shim for generously sharing rAAV9-amiR-ctrl and rAAV9-amiR-Shn3 plasmids with us. We also thank Flow Cytometry Platform and Imaging Center at Core Facility of Biomedical Sciences in Xiamen University for their experimental assistance. And we appreciate Xiamen University Laboratory Animal Center for their kind help with animal administration. This project was supported by the National Natural Science Foundation of China (81972034, 92068104 and 82002262 to R.X.), the National Key R&D Program of China (2020YFA0112900 to R.X.) and Project of Xiamen Cell Therapy Research Center (3502220214001 to R.X.). M.B.G. was also supported by a the NIH grant of US (R01AR075585, R01HD115274, R01CA282815 to M.B.G.), Career Award for Medical Scientists from the Burroughs Wellcome Fund and a Pershing Square Sohn Cancer Research Alliance and the Maximizing Innovation in Neuroscience Discovery (MIND) Prize. S.B. is supported by a JumpStart Research Career Development Award from Weill Cornell Medicine and a Study Abroad Scholarships from the Mogam Science Scholarship Foundation.

AUTHOR CONTRIBUTIONS

R.X. supervised this project. R.X., N.L. and M.B.G. designed the research and wrote the manuscript. N.L., B.S., Z.L., J.H., J.S., A.R.Y., S.B., S.X., Z.W., R.H. and Y.C. performed research. H.H. performed tissue clearing and imaging. Y.X., T.Q. and H.Z. assisted flow cytometry and FACS. R.S. supported animal studies and management. B.S., Z.L., L.M. and J.H. analyzed data.

ADDITIONAL INFORMATION

Supplementary information The online version contains supplementary material available at <https://doi.org/10.1038/s41413-024-00349-1>.

Competing interests: The authors declare no competing interests.

REFERENCES

- Marini, J. C. et al. Osteogenesis imperfecta. *Nat. Rev. Dis. Prim.* **3**, 17052 (2017).
- Rauch, F. & Glorieux, F. H. Osteogenesis imperfecta. *Lancet* **363**, 1377–1385 (2004).
- Palomo, T. et al. Intravenous bisphosphonate therapy of young children with osteogenesis imperfecta: skeletal findings during follow up throughout the growing years. *J. Bone Miner. Res.* **30**, 2150–2157 (2015).
- Glorieux, F. H. et al. Cyclic administration of pamidronate in children with severe osteogenesis imperfecta. *N. Engl. J. Med.* **339**, 947–952 (1998).

- Orwoll, E. S. et al. Evaluation of teriparatide treatment in adults with osteogenesis imperfecta. *J. Clin. Investig.* **124**, 491–498 (2014).
- Sinder, B. P. et al. Sclerostin antibody improves skeletal parameters in a *Brl/+* mouse model of osteogenesis imperfecta. *J. Bone Miner. Res.* **28**, 73–80 (2013).
- Bradbury, L. A. et al. Risedronate in adults with osteogenesis imperfecta type I: increased bone mineral density and decreased bone turnover, but high fracture rate persists. *Osteoporos. Int.* **23**, 285–294 (2012).
- Munns, C. F., Rauch, F., Zeitlin, L., Fassier, F. & Glorieux, F. H. Delayed osteotomy but not fracture healing in pediatric osteogenesis imperfecta patients receiving pamidronate. *J. Bone Miner. Res.* **19**, 1779–1786 (2004).
- Rajzbaum, G. et al. Treatment persistence and changes in fracture risk, back pain, and quality of life amongst patients treated with teriparatide in routine clinical care in France: results from the European Forsteo Observational Study. *Jt. Bone Spine* **81**, 69–75 (2014).
- Cardinal, M. et al. Sclerostin antibody reduces long bone fractures in the *oim/oim* model of osteogenesis imperfecta. *Bone* **124**, 137–147 (2019).
- Dwan, K., Phillipi, C. A., Steiner, R. D. & Basel, D. Bisphosphonate therapy for osteogenesis imperfecta. *Cochrane Database Syst. Rev.* **10**, Cd005088 (2016).
- Song, I. W. et al. Targeting TGF- β for treatment of osteogenesis imperfecta. *J. Clin. Invest.* **132**, e152571 (2022).
- Fukuda, T. et al. Sema3A regulates bone-mass accrual through sensory innervations. *Nature* **497**, 490–493 (2013).
- Xu, R. et al. Targeting skeletal endothelium to ameliorate bone loss. *Nat. Med.* **24**, 823–833 (2018).
- Ben Shoham, A. et al. Deposition of collagen type I onto skeletal endothelium reveals a new role for blood vessels in regulating bone morphology. *Development* **143**, 3933–3943 (2016).
- Sivaraj, K. K. & Adams, R. H. Blood vessel formation and function in bone. *Development* **143**, 2706–2715 (2016).
- Chan, C. K. et al. Identification and specification of the mouse skeletal stem cell. *Cell* **160**, 285–298 (2015).
- Debnath, S. et al. Discovery of a periosteal stem cell mediating intramembranous bone formation. *Nature* **562**, 133–139 (2018).
- Jones, D. C. et al. Regulation of adult bone mass by the zinc finger adapter protein Schnurri-3. *Science* **312**, 1223–1227 (2006).
- Morris, J. A. et al. An atlas of genetic influences on osteoporosis in humans and mice. *Nat. Genet.* **51**, 258–266 (2019).
- Li, N. et al. Osteoclasts are not a source of SLIT3. *Bone Res.* **8**, 11 (2020).
- Chipman, S. D. et al. Defective pro alpha 2(I) collagen synthesis in a recessive mutation in mice: a model of human osteogenesis imperfecta. *Proc. Natl. Acad. Sci. USA* **90**, 1701–1705 (1993).
- Kusumbe, A. P., Ramasamy, S. K. & Adams, R. H. Coupling of angiogenesis and osteogenesis by a specific vessel subtype in bone. *Nature* **507**, 323–328 (2014).
- Helbling, P. M. et al. Global transcriptomic profiling of the bone marrow stromal microenvironment during postnatal development, aging, and inflammation. *Cell Rep.* **29**, 3313–3330.e14 (2019).
- Xu, C. et al. Stem cell factor is selectively secreted by arterial endothelial cells in bone marrow. *Nat. Commun.* **9**, 2449 (2018).
- Roelofs, A. J. et al. Identification of the skeletal progenitor cells forming osteophytes in osteoarthritis. *Ann. Rheum. Dis.* **79**, 1625–1634 (2020).
- Ambrosi, T. H. et al. Aged skeletal stem cells generate an inflammatory degenerative niche. *Nature* **597**, 256–262 (2021).
- Mizuhashi, K. et al. Resting zone of the growth plate houses a unique class of skeletal stem cells. *Nature* **563**, 254–258 (2018).
- Worthley, D. L. et al. Gremlin 1 identifies a skeletal stem cell with bone, cartilage, and reticular stromal potential. *Cell* **160**, 269–284 (2015).
- Marom, R., Lee, Y. C., Grafe, I. & Lee, B. Pharmacological and biological therapeutic strategies for osteogenesis imperfecta. *Am. J. Med. Genet. C Semin. Med. Genet.* **172**, 367–383 (2016).
- Shim, J. H. et al. Schnurri-3 regulates ERK downstream of WNT signaling in osteoblasts. *J. Clin. Investig.* **123**, 4010–4022 (2013).
- Ambrosi, T. H. et al. Distinct skeletal stem cell types orchestrate long bone skeletogenesis. *eLife*. **10**, e66063 (2021).
- Amoasii, L. et al. Gene editing restores dystrophin expression in a canine model of Duchenne muscular dystrophy. *Science* **362**, 86–91 (2018).
- Chemello, F., Bassel-Duby, R. & Olson, E. N. Correction of muscular dystrophies by CRISPR gene editing. *J. Clin. Investig.* **130**, 2766–2776 (2020).
- Frangoul, H. et al. CRISPR-Cas9 gene editing for sickle cell disease and β -thalassaemia. *N. Engl. J. Med.* **384**, 252–260 (2021).
- Yang, Y. S. et al. Bone-targeting AAV-mediated silencing of Schnurri-3 prevents bone loss in osteoporosis. *Nat. Commun.* **10**, 2958 (2019).
- Tevlin, R. et al. Pharmacological rescue of diabetic skeletal stem cell niches. *Sci. Transl. Med.* **9**, eaag2809 (2017).

38. Murphy, M. P. et al. Articular cartilage regeneration by activated skeletal stem cells. *Nat. Med.* **26**, 1583–1592 (2020).
39. Alcorta-Sevillano, N., Infante, A., Macías, I. & Rodríguez, C. I. Murine animal models in osteogenesis imperfecta: the quest for improving the quality of life. *Int. J. Mol. Sci.* **24**, 184 (2023).
40. Shen, B. et al. A mechanosensitive peri-arteriolar niche for osteogenesis and lymphopoiesis. *Nature* **591**, 438–444 (2021).
41. Matsushita, Y. et al. A Wnt-mediated transformation of the bone marrow stromal cell identity orchestrates skeletal regeneration. *Nat. Commun.* **11**, 332 (2020).
42. Xie, H. et al. PDGF-BB secreted by preosteoclasts induces angiogenesis during coupling with osteogenesis. *Nat. Med.* **20**, 1270–1278 (2014).
43. Xu, R. et al. c-Jun N-terminal kinases (JNKs) are critical mediators of osteoblast activity in vivo. *J. Bone Miner. Res.* **32**, 1811–1815 (2017).
44. Kusumbe, A. P., Ramasamy, S. K., Starsichova, A. & Adams, R. H. Sample preparation for high-resolution 3D confocal imaging of mouse skeletal tissue. *Nat. Protoc.* **10**, 1904–1914 (2015).
45. Nudell, V. et al. HYBRiD: hydrogel-reinforced DISCO for clearing mammalian bodies. *Nat. Methods* **19**, 479–485 (2022).
46. Wang, Q., Liu, K., Yang, L., Wang, H. & Yang, J. BoneClear: whole-tissue immunolabeling of the intact mouse bones for 3D imaging of neural anatomy and pathology. *Cell Res.* **29**, 870–872 (2019).



Open Access This article is licensed under a Creative Commons Attribution 4.0 International License, which permits use, sharing, adaptation, distribution and reproduction in any medium or format, as long as you give appropriate credit to the original author(s) and the source, provide a link to the Creative Commons licence, and indicate if changes were made. The images or other third party material in this article are included in the article's Creative Commons licence, unless indicated otherwise in a credit line to the material. If material is not included in the article's Creative Commons licence and your intended use is not permitted by statutory regulation or exceeds the permitted use, you will need to obtain permission directly from the copyright holder. To view a copy of this licence, visit <http://creativecommons.org/licenses/by/4.0/>.

© The Author(s) 2024